Check for updates

Water Resources Research

RESEARCH ARTICLE
10.1029/2026WR044004

Coupling MRI and XRCT to Resolve Structure–Transport Evolution During Enzyme-Induced Calcite Precipitation at the REV Scale

Samira Emadi[1], **Puyan Bakhshi**[1], **Andreas Pohlmeier**[1], **and Johan Alexander Huisman**[1]

[1]Agrosphere (IBG-3), Institute of Bio- and Geosciences, Forschungszentrum Jülich GmbH, Jülich, Germany

Key Points:

- Permeability dropped by more than three orders of magnitude during EICP treatment, while porosity declined only moderately
- Combined magnetic resonance imaging and X-ray computed tomography resolved where precipitation formed and how it changed flow behavior
- Early flow reduction was driven by pore throat blockage and connectivity loss before widespread pore body narrowing

Supporting Information:

Supporting Information may be found in the online version of this article.

Correspondence to:

S. Emadi,
s.emadi@fz-juelich.de

Citation:

Emadi, S., Bakhshi, P., Pohlmeier, A., & Huisman, J. A. (2026). Coupling MRI and XRCT to resolve structure–transport evolution during enzyme-induced calcite precipitation at the REV scale. *Water Resources Research*, *62*, e2026WR044004. https://doi.org/10.1029/2026WR044004

Received 20 MAR 2026
Accepted 16 OCT 2026

Author Contributions:

Conceptualization: Samira Emadi, Andreas Pohlmeier, Johan Alexander Huisman
Data curation: Samira Emadi, Puyan Bakhshi
Formal analysis: Samira Emadi, Puyan Bakhshi
Investigation: Samira Emadi
Methodology: Samira Emadi, Puyan Bakhshi, Andreas Pohlmeier, Johan Alexander Huisman

© 2026 The Author(s). *Water Resources Research* published by Wiley Periodicals LLC on behalf of American Geophysical Union.
This is an open access article under the terms of the Creative Commons Attribution License, which permits use, distribution and reproduction in any medium, provided the original work is properly cited.

Abstract The aim of this study is to understand how enzyme-induced calcite precipitation (EICP) modifies flow and transport in porous media, as this is essential for developing sustainable approaches to soil stabilization, permeability control, and groundwater management. For this, we investigated the coupled evolution of pore structure and hydraulic properties during EICP at the representative elementary volume (REV) scale using a dual non-invasive imaging approach combining X-ray computed tomography (XRCT) and magnetic resonance imaging (MRI). Three replicate sand columns with initial permeabilities between 22×10^{-12} m^2 and 25×10^{-12} m^2 were treated with EICP using a constant flow injection and solutions of 0.5 M $CaCl_2$, 0.5 M urea, and 5.0 g L^{-1} jack bean meal. Over six injection cycles (175 pore volumes), permeability decreased by more than three orders of magnitude, while average porosity declined moderately from 0.38 to 0.28. XRCT revealed that precipitation was concentrated near the inlet, where the surface to volume ratio increased from 0.055 to 0.065 μm^{-1} and tortuosity rose from ∼2.0 to ∼3.5. MRI measurements showed corresponding localized reductions in water content and relaxation times, with T_1 decreasing from ∼1.5 to ∼1.0 s and T_2 from ∼50 to ∼30 ms. The combined imaging results indicate a two-stage precipitation process with early pore-throat blockage followed by progressive narrowing of pore bodies. These findings demonstrate that permeability loss is governed not only by porosity reduction but also by precipitation distribution.

Plain Language Summary When minerals form inside the small spaces between sand grains, they can strongly change how easily water flows through the material. Understanding this process is important for groundwater management and for subsurface engineering methods that use mineral formation to reduce leakage or control flow. In this study, we tracked how mineral buildup changed both the structure of a sand column and its ability to transmit water during treatment. We combined two non-invasive imaging methods that provide complementary information. X-ray imaging showed changes in the pore structure, while magnetic resonance imaging showed changes in water distribution and water behavior inside the pores. We also measured permeability, which describes how easily water can flow through the sample. We found that water flow decreased by more than 1,000 times, even though total pore space decreased much less. This means that flow reduction was controlled mainly by where minerals formed and how they blocked pore connections, not simply by the overall amount of pore space lost. These results help improve predictions of flow changes in treated porous materials.

1. Introduction

Soil stabilization and hydraulic control remain critical challenges in geotechnical and environmental engineering. Tens of thousands of improvement projects are implemented annually, at costs of billions of dollars, with most relying on conventional mechanical methods (e.g., compaction, preloading) or chemical stabilizers such as cement and lime grouts (Arab et al., 2021; Cheng et al., 2017). While effective, these methods are energy intensive, costly, and environmentally damaging due to CO_2 emissions and chemical residues (DeJong et al., 2014). As a result, there is growing demand for more sustainable alternatives.

Bio-cementation, which exploits biological or biochemical pathways to induce calcium carbonate ($CaCO_3$) precipitation, has emerged as a promising technology (DeJong et al., 2010; Krajewska, 2018). Two main approaches have been developed: microbially induced calcite precipitation (MICP), in which ureolytic bacteria such as *Sporosarcina pasteurii* hydrolyze urea to produce carbonate and ammonia (Cuthbert et al., 2013; Kavazanjian & Hamdan, 2015) and enzyme-induced calcite precipitation (EICP), where urease enzymes directly catalyze urea hydrolysis without the complexity of using living cells. The concept of using plant-derived urease enzymes for

Project administration: Johan Alexander Huisman
Resources: Andreas Pohlmeier, Johan Alexander Huisman
Software: Puyan Bakhshi
Supervision: Andreas Pohlmeier, Johan Alexander Huisman
Validation: Puyan Bakhshi
Visualization: Samira Emadi
Writing – original draft: Samira Emadi
Writing – review & editing: Puyan Bakhshi, Andreas Pohlmeier, Johan Alexander Huisman

carbonate biomineralization was first proposed by Nemati and Voordouw (2003), with subsequent studies demonstrating increased stiffness and permeability reduction in sands treated with EICP (Ahenkorah et al., 2020; Almajed et al., 2018; Yasuhara et al., 2012).

By modifying the pore space, $CaCO_3$ precipitation can substantially alter water retention, permeability, and flow pathways. These changes are typically described by shifts in capillary pressure-saturation relationships and porosity-permeability relationships (Hommel et al., 2022; Weinhardt et al., 2022; Zhang et al., 2023). However, significant knowledge gaps remain in understanding how precipitation evolves within three-dimensional porous media and how this affects flow and transport in realistic flow conditions. Many laboratory studies relied on batch or simple one-dimensional column experiments (Cheng & Cord-Ruwisch, 2014; Hu et al., 2021), which provide valuable mechanistic insights but do not resolve the internal 3D structure of the porous medium during treatment. Even in flow-through columns, precipitation is frequently inferred indirectly from outlet chemistry or end-point measurements rather than observed directly (Arab et al., 2021; Kakelar et al., 2016).

Recent advances in high resolution imaging offer new possibilities for quantifying biomineralization processes. Magnetic resonance imaging (MRI) allows to non-destructively map the evolving distribution of water content and relaxation times (T_1, T_2), which are sensitive to pore size distribution, surface interactions, and mineral deposition (Duschl et al., 2015; Haber-Pohlmeier et al., 2021; Thrane et al., 2020), and thus are dynamic proxies for pore space evolution. X-ray computed tomography (XRCT) allows to resolve the evolving 3D pore architecture and mineral phases, enabling calculation of porosity, surface to volume ratios, and tortuosity (Cnudde & Boone, 2013; Guan et al., 2019; Salek & Beckingham, 2023; Wildenschild & Sheppard, 2013). These metrics also directly reflect transport and reaction processes: porosity governs flow capacity, tortuosity reduces permeability and increases residence times by elongating transport pathways, and S/V ratios control the availability of reactive interfaces.

Although non-invasive imaging has been applied to biomineralization, its use in MICP and EICP remains relatively limited. Kirkland et al. (2019) used XRCT to quantify sealing of a channel defect during MICP. Yang et al. (2024) combined XRCT with hydraulic measurements to relate local MICP-induced deposition to flow redistribution and permeability changes, while Kwon et al. (2024) used XRCT to resolve pore-scale precipitation patterns in MICP-treated sands of different grain sizes and linked these to grain-scale cementation strength. MRI studies have mainly targeted dynamic hydrological signatures and pore-scale evolution during biomineralization. For example, Handley-Sidhu et al. (2013) used one- and two-dimensional MRI to monitor calcium carbonate precipitation in situ, and Fridjonsson et al. (2011) employed high-field nuclear magnetic resonance (NMR) measurements to quantify changes in hydrodynamic dispersion in a packed-bead model system undergoing MICP. Sham et al. (2013) combined MRI and NMR displacement measurements to monitor MICP in borosilicate beads and sandstone, obtaining spatial distributions of precipitate and flow. Kirkland et al. (2017) used a low-field NMR well-logging tool to monitor MICP in a sand-filled bioreactor, tracking NMR signal amplitude and T_2 relaxation and imaging. Thrane et al. (2020) used a 2-MHz rock core analyzer to measure T_2 relaxation in different granular media, observing systematic increases in T_2 with MICP progression.

Only a limited number of studies have combined non-invasive imaging techniques to investigate biomineralization in porous media. Bray et al. (2017) employed MRI together with XRCT to study $CaCO_3$ precipitation induced by solution mixing, where MRI was used to map velocity and dispersion fields and XRCT was used to visualize precipitate localization. While this work demonstrated the complementarity of the two methods, structural and transport information were not quantitatively co-registered at the representative elementary volume (REV) scale, nor was the progressive evolution of pore structure, permeability, and relaxation behavior resolved. More recently, Willett et al. (2024) combined low-field NMR and XRCT to assess the extent of biomineralization in MICP-treated sands. However, the NMR measurements provided bulk-averaged relaxation responses without spatial resolution, and the evolution of the permeability was not tracked in parallel with imaging. As a result, derived links between spatially resolved microstructural changes and hydraulic response remained indirect. Overall, existing studies have so far employed XRCT to characterize pore structure and mineral distribution, while MRI or NMR was used to probe fluid-phase behavior. A fully integrated and spatially co-registered analysis that directly couples REV-scale structural evolution (porosity, tortuosity, surface-to-volume ratio) with transport-sensitive MRI parameters (water content, T_1, T_2) during progressive EICP treatment has not yet been reported.

In this study, we address this gap by coupling XRCT and MRI to investigate EICP in sand columns. By combining these imaging modalities with permeability monitoring, we directly link precipitation patterns to evolving

19447973, 2026, 11, Downloaded from https://agupubs.onlinelibrary.wiley.com/doi/10.1029/2026WR044004 by Sander Huisman - Forschungszentrum Juelich Gmbh , Wiley Online Library on [01/11/2026]. See the Terms and Conditions (https://onlinelibrary.wiley.com/terms-and-conditions) on Wiley Online Library for rules of use; OA articles are governed by the applicable Creative Commons License

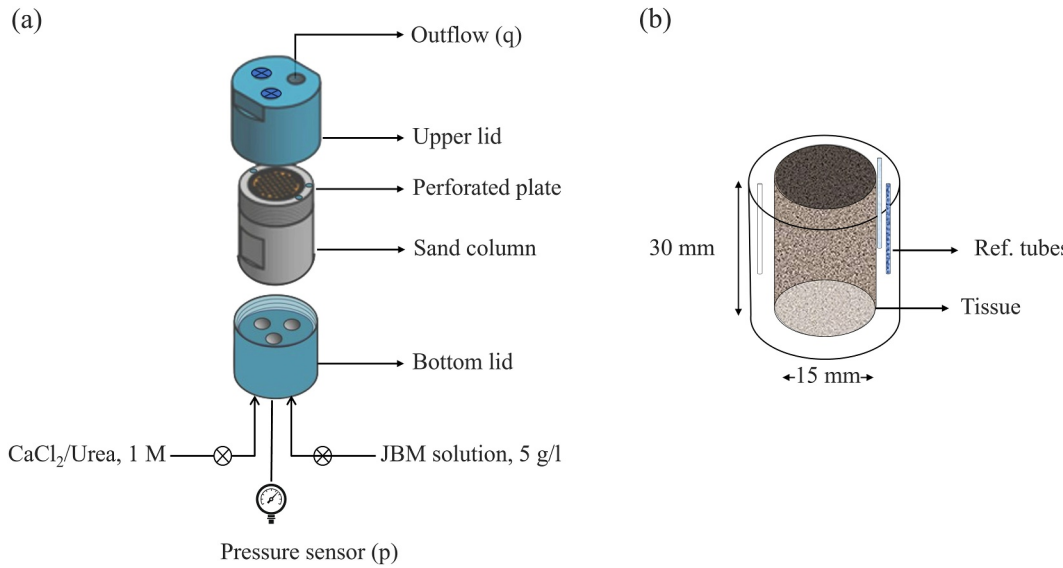


Figure 1. Schematic illustration of the PMMA sample holder packed with sand and ports for fluid injection and pressure measurements. (a) Sample holder with three ports at the bottom of the column (inlet), two connected to a dual-syringe pump containing enzyme and cementing solution, and the last one connected to a pressure sensor. (b) Dimensions of sample.

hydraulic properties. This integrated workflow establishes a methodological framework for advancing bio-cementation research at the representative elementary volume (REV) scale.

2. Materials and Methods

2.1. Sample and Solution Preparation

EICP requires a source of calcium and carbonate ions, as well as urease to catalyze urea hydrolysis. In this study, we used calcium chloride ($CaCl_2$) and urea as reactants, while Jack Bean meal (JBM) provided the urease enzyme. Because ureolysis proceeds rapidly even at ambient temperature, premature mixing of all components can cause uncontrolled precipitation. To avoid this, the cementing and enzyme solutions were prepared separately and mixed in equal amounts inside the bottom lid of the sample holder during injection (see Figure 1). The cementing solution consisted of 1.0 mol/L urea and 1.0 mol/L $CaCl_2{\cdot}2H_2O$ (Merck KGaA, Germany). The enzyme solution was obtained by suspending 5.0 g of jack bean meal (MP Biomedicals, USA) in 1.0 L of deionized water, followed by overnight stirring at room temperature. The extract was filtered through 20 μm filter paper to remove coarse particulates, leaving a stable enzyme-rich suspension. For permeability characterization and column saturation, a diluted cementing solution (0.5 mol/L urea and 0.5 mol/L $CaCl_2$) was used to minimize uncontrolled precipitation while preserving ionic strength.

Custom-designed sample holders were constructed from polymethylmethacrylate (PMMA) with an inner diameter of 15 mm and a maximum filling height of 30 mm (Figure 1b). The sample holder was equipped with three inlets, allowing independent connection to a dual-syringe pump delivering the cementing and the enzyme solution as well as an external pressure gauge (Cetoni GmbH, Korbussen, Germany; range 0–2 bar). The pressure sensor measured gauge pressure at the column inlet, while the outlet was open to ambient pressure. Therefore, the recorded pressure corresponds to the pressure drop (ΔP) across the sand column. Constant flow was maintained using a Nemesys mid-pressure syringe pump (CETONI GmbH, Korbussen, Germany). Flow distribution within the column was homogenized by perforated plates (1.0 mm holes) placed at both ends of the sand pack, while tissues prevented sand grains from clogging the perforated plates (Figure 1a).

For quantitative MRI calibration, three external holes of 1 mm ID were drilled into the outer wall of the PMMA cylinder (Figure 1). These holes were filled with half-concentrated cementing solution (0.5 M $CaCl_2$ + 0.5 M urea), a mixture of 70% H_2O and 30% D_2O (v/v), and deionized water after sample preparation. These served as calibration standards for bulk water contents of 100%, 70%, and 100%, respectively. We used the signal intensities

19447973, 2026, 11, Downloaded from https://agupubs.onlinelibrary.wiley.com/doi/10.1029/2026WR044004 by Sander Huisman - Forschungszentrum Juelich Gmbh , Wiley Online Library on [01/11/2026]. See the Terms and Conditions (https://onlinelibrary.wiley.com/terms-and-conditions) on Wiley Online Library for rules of use; OA articles are governed by the applicable Creative Commons License

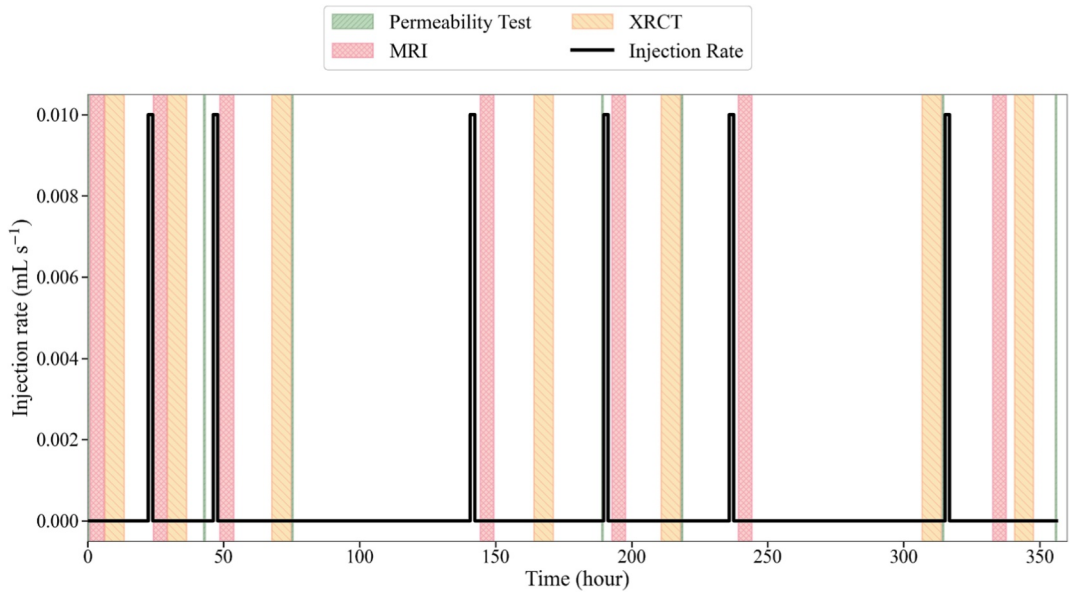


Figure 2. Exemplary timeline of the EICP-1 experiment with a constant flow rate (0.01 mL s^{-1}) and intervals of MRI, XRCT, and permeability measurements. Color-shaded boxes indicate MRI, XRCT and permeability measurements, the black line indicates the injection rate.

from the reference tubes to normalize MRI data and to calculate water content within the sand pack. The reference tubes were also used to co-register XRCT and MRI images.

To assess the reproducibility of EICP, three replicate columns were prepared, EICP-1, EICP-2, and EICP-3 using F32 quartz sand (Quarzwerke GmbH, Frechen, Germany). This is a processed natural quartz sand with a chemical purity of SiO_2 > 99%, a mean grain size of 0.24 mm, and 93% of the particle diameters between 0.125 and 0.355 mm according to manufacturer specifications. The three samples were prepared using a dry-packing approach where dry F32 sand was filled into the sample holders in layers with tapping and light tamping applied between layers to achieve a uniform cavity-free distribution. This procedure was developed through iterative trial packings and was found to reliably yield a target porosity of ∼0.40. The approximate sand mass required to fill the ∼20 mm target column height at this porosity was estimated in advance. The exact initial porosity of each replicate was then determined to provide a baseline for assessing structural changes induced by EICP. For this, dry sand mass was obtained by weighing the sample holder before and after packing, while sample height and diameter were extracted from XRCT images.

The samples were saturated initially with a diluted cementing solution (0.5 M $CaCl_2$ + 0.5 M urea). Saturation was achieved by placing the sample in an open vessel filled with the solution inside a desiccator connected to a vacuum pump. After 20 min of applying a weak vacuum (up to 35 mbar), the valve was released and the sample remained submerged for an additional 10 min to ensure complete saturation. A short qualitative MRI or XRCT scan was used to confirm homogeneous saturation and the absence of trapped air bubbles.

2.2. EICP Experiments

EICP experiments were performed by co-injecting the cementing and enzyme solutions into the sample holders prepared with sand, using a combined constant flow rate of 0.01 mL s^{-1}, corresponding to a Darcy velocity of ∼0.063 mm s^{-1}. A total of ∼175 pore volumes (PV) of solution was delivered over six injection cycles. Each injection cycle was followed by non-invasive imaging using both MRI and XRCT, after which the intrinsic permeability was determined. This cycle-based design enabled direct comparison of evolving hydraulic and structural properties. The experimental timeline is summarized in Figure 2. The injection experiments were performed in triplicate under nominally identical conditions to capture the inherent stochasticity of the EICP process. Due to the coupled nature of flow and precipitation, slight variations in local pore structure and reaction kinetics can lead to divergent evolution paths even under identical boundary conditions.

19447973, 2026, 11, Downloaded from https://agupubs.onlinelibrary.wiley.com/doi/10.1029/2026WR044004 by Sander Huisman - Forschungszentrum Juelich Gmbh , Wiley Online Library on [01/11/2026]. See the Terms and Conditions (https://onlinelibrary.wiley.com/terms-and-conditions) on Wiley Online Library for rules of use; OA articles are governed by the applicable Creative Commons License

19447973, 2026, 11, Downloaded from https://agupubs.onlinelibrary.wiley.com/doi/10.1029/2026WR044004 by Sander Huisman - Forschungszentrum Juelich Gmbh , Wiley Online Library on [01/11/2026]. See the Terms and Conditions (https://onlinelibrary.wiley.com/terms-and-conditions) on Wiley Online Library for rules of use; OA articles are governed by the applicable Creative Commons License

2.3. Permeability Measurements

The intrinsic permeability was determined before EICP treatment and after each injection cycle. Measurements were performed by injecting a diluted cementing solution (0.5 M $CaCl_2$ + 0.5 M urea) at four flow rates (0.002, 0.004, 0.006, and 0.008 mL s^{-1}) that were lower than those used during EICP injection (0.01 mL s^{-1}). These reduced flow rates were used to avoid mobilization of freshly formed precipitates to the extent possible. For each flow rate, the resulting pressure drop across the sample was recorded with a high-precision pressure sensor (Cetoni GmbH, Korbussen, Germany; range 0–2 bar). By plotting the recorded pressure drop as a function of flow rate, the permeability was determined using:

$$k = \frac{\mu \cdot L}{A \cdot \left(\frac{\Delta p}{\Delta Q}\right)}, \tag{1}$$

where k is the intrinsic permeability, μ is the fluid viscosity, L is the sample length, A is the cross-sectional area, and $\Delta p/\Delta Q$ is the slope of the pressure and flow relationship. An example of a permeability determination is provided in Figure S1 of Supporting Information S1 Effluent calcium concentration was not measured during permeability testing. We note, however, that no deviations from linearity were observed in the pressure–flow relationships obtained in this study, which would be expected if dissolution or precipitation occurred appreciably during the test itself. Nevertheless, we recommend that future studies incorporate effluent chemistry monitoring to directly confirm this.

The dynamic viscosity of the EICP solution components required to obtain the permeability was determined at room temperature (~25°C) using a rolling-ball microviscometer (Lovis 2000 M, Anton Paar GmbH, Austria). Viscosity measurements were performed on solutions with (a) 1.0 M $CaCl_2$ + 1.0 M urea, (b) 0.5 M $CaCl_2$ + 0.5 M urea, (c) 5 g L^{-1} JBM (filtered), and (d) 0.5 M $CaCl_2$ + 0.5 M urea with 2.5 g L^{-1} JBM. The latter mixed solution reflects the solution after injection, and viscosity was recorded 10 min after preparation to capture its early-stage rheological properties. The obtained viscosity of the 1.0 M $CaCl_2$ + 1.0 M urea solution was 1.472 mPa.s, which decreased to 1.23 mPa.s for 0.5 M CaCl2 + 0.5 M urea solution. The viscosity of the enzyme solution was 1.06 mPa.s. The mixed cementing-enzyme solution exhibited an intermediate viscosity of 1.33 mPa.s. To determine the permeability in this study, the measured viscosity of the 0.5 M $CaCl_2$/urea cementing solution (~1.23 mPa.s) was used because this solution was used during the permeability determination.

2.4. MRI Imaging

Magnetic resonance imaging (MRI) was used to non-invasively monitor changes in the water phase before EICP and after each injection cycle. MRI detects signals from hydrogen nuclei in water molecules and provides spatially resolved information on water content and relaxation behavior, which is sensitive to pore geometry and mineral deposition. In porous media, the longitudinal (T_1) and transverse (T_2) relaxation times shorten as pore size decreases or surface relaxivity increases, allowing indirect characterization of precipitation-induced structural changes.

All MRI measurements were conducted using a Bruker MRI scanner with an inserted wide bore (WB) gradient system operating at $B_0 = 4.7$ T with a maximum gradient strength of 1.4 T/m. T_1 relaxation was measured using a RAREVTR (Rapid Acquisition with Relaxation Enhancement, Variable Time of Repetition) pulse sequence. Eight echoes were recorded with an inter-echo spacing of 3.5 ms, and eight repetition times were exponentially distributed between 500 ms and 10,000 ms. The field of view (FOV) was 20 × 36 mm^2, and five vertical slices of 0.5 mm thickness and a 1.78 mm inter-slice gap were acquired. T_2 relaxation was determined using a MSME (Multi-Slice Multi-Echo) pulse sequence with an echo time of 3.2 ms, 128 echoes, and a repetition time of 8,000 ms. The FOV was 20 × 30 mm^2, and five vertical slices of 0.5 mm thickness and a 1.78 mm inter-slice gap were acquired. Water content (WC) was also quantified using the MSME sequence based on signal amplitude, which is directly proportional to the number of hydrogen protons in the voxel volume. Two acquisition strategies were applied to capture both horizontal and vertical water content distributions. For horizontal mapping, 27 axial slices were acquired at an echo time of 3.0 ms and a repetition time of 15,000 ms (FOV: 20 × 20 mm^2, slice thickness: 0.5 mm, gap: 0.1 mm). For vertical mapping, the same MSME sequence and parameters were used with

19447973, 2026, 11, Downloaded from https://agupubs.onlinelibrary.wiley.com/doi/10.1029/2026WR044004 by Sander Huisman - Forschungszentrum Juelich Gmbh , Wiley Online Library on [01/11/2026]. See the Terms and Conditions (https://onlinelibrary.wiley.com/terms-and-conditions) on Wiley Online Library for rules of use; OA articles are governed by the applicable Creative Commons License

Table 1
Overview of the Pulse Sequences and Associated Settings for T_1, T_2, and Water Content Measurements With MRI

Parameter	T_1	T_2	Water content (vertical)	Water content (horizontal)
Pulse sequence	RAREVTR	MSME	MSME	MSME
T_E (ms)	12.36	3.2	3	3
T_R (ms)	500–10,000	8000	15,000	15,000
Number of slices	5	5	27	27
Slice orientation	Vertical	Vertical	Vertical	Axial
Slice thickness (mm)	0.5	0.5	0.5	0.6
Number of averages	4	2	2	2
Total scan time (min)	37	68	96	96
Field of view (mm^2)	20×36	20×30	20×20	20×36
Matrix size	192×256	256×256	192×192	192×256

Note. T_E is the echo time, T_R is the repetition time, T_1 and T_2 are longitudinal and transverse relaxation times, respectively.

an adjusted FOV of 20×36 mm^2 to ensure full coverage of the entire column height. Table 1 summarizes all MRI acquisition parameters. Additional information on the pulse sequences can be found in Nitz (1999).

Image reconstruction for T_1 and T_2 determination involved Fourier transformation, filtering, and complex division, performed in IDL (Harris Geospatial, USA). Visualization and post-processing, including normalization and ROI extraction, were conducted in Fiji (Schindelin et al., 2012). Water content images were reconstructed using the Bruker Paravision pipeline, and normalized to the reference tube containing 0.5 M $CaCl_2$ + 0.5 M urea to scale voxel intensities between 0 and 1.

The T_1 and T_2 measurements obtained with MRI were interpreted using the Brownstein–Tarr model (Brownstein & Tarr, 1979). In this biphasic exchange framework, the pore water is divided into a bulk region and a thin surface layer that rapidly exchanges by molecular diffusion. Relaxation is accelerated at the solid–liquid interface due to restricted molecular motion and local magnetic field inhomogeneities arising from susceptibility contrasts and paramagnetic centers. The overall relaxation rates can be expressed as:

$$\frac{1}{T_1} = \frac{1}{T_{1,\text{bulk}}} + \rho_1 \frac{S}{V}, \tag{2}$$

and

$$\frac{1}{T_2} = \frac{1}{T_{2,\text{bulk}}} + \rho_2 \frac{S}{V} + \frac{1}{T_{2,\text{diffusion}}}, \tag{3}$$

where S/V is the pore surface-to-volume ratio, and ρ_1 and ρ_2 are the surface relaxivities for T_1 and T_2, respectively. The additional diffusion term for T_2 relaxation accounts for transverse precessing magnetization in magnetic field gradients, and can be approximated in the short-time limit (Mitchell et al., 2010) by the Bloch–Torrey expression:

$$1/T_{2,\text{diffusion}} = (\gamma\, g)^2 D_0\, t_E^2/12, \tag{4}$$

where γ is the gyromagnetic ratio, g is the effective gradient, D_0 is the self-diffusion coefficient, and t_E is the echo time. This expression is included here to illustrate the physical origin of diffusion-driven transverse relaxation and to support the qualitative interpretation of T_2 changes in terms of evolving pore geometry and confinement. However, under the long echo-time imaging conditions used in this study, the short-time approximation underlying Equation 4 is not fully valid, and therefore the diffusion term was not explicitly included in the quantitative analysis (Mitchell et al., 2010). In addition to the internal-gradient diffusion described above, an additional contribution to the effective T_2 can arise from diffusion in the imaging read (spatial-encoding) gradient

19447973, 2026, 11, Downloaded from https://agupubs.onlinelibrary.wiley.com/doi/10.1029/2026WR044004 by Sander Huisman - Forschungszentrum Juelich Gmbh , Wiley Online Library on [01/11/2026]. See the Terms and Conditions (https://onlinelibrary.wiley.com/terms-and-conditions) on Wiley Online Library for rules of use; OA articles are governed by the applicable Creative Commons License

during signal acquisition (Edzes et al., 1998). Using Equation 6 of Edzes et al. (1998) and our acquisition parameters (in-plane resolution 0.117 mm, acquisition window 1.7 ms, $t_E = 3.2$ ms, $D \leq 2 \times 10^{-9}$ m^2 s^{-1}), this contribution is estimated to be $1/T_2'' \approx 1.6$ s^{-1}, which is small relative to the measured relaxation rates in this study ($1/T_2 > 10$ s^{-1}). We therefore consider this effect to be of secondary importance here, and did not further consider it. For systems with substantially longer T_2, this effect is more significant and needs to be considered.

2.5. XRCT Imaging

All XRCT measurements were carried out using a CT-COMPACT system (ProCon X-Ray GmbH, Sarstedt, Germany). Scanning was performed at a source voltage of 130 kV and a current of 61 μA, corresponding to a power of 7.9 W. Each projection was acquired with an exposure time of 2.5 s, followed by a 0.2° rotation step, until 1800 projections were collected over a 360° rotation. This procedure was repeated with a shifted stage elevation to capture the entire sample volume. The nominal pixel size for all scans was 8 μm. This corresponds to approximately 30 voxels across the mean grain diameter of the F32 sand used (0.24 mm; Section 2.1), and at least ∼11 voxels for the finest sieve fraction (0.090–0.125 mm). This is well above commonly applied thresholds for reliable segmentation of grain and pore boundaries (Saxena et al., 2018).

Raw projection data were reconstructed using VGSTUDIO (Volume Graphics GmbH, Heidelberg, Germany) and subsequently processed and analyzed in Dragonfly (Comet Technologies Canada Inc., Montréal, Canada). After normalizing the images, a denoising filter was applied with parameters optimized to minimize noise, while maintaining sharpness. After stitching the top and bottom scans of each sample, the pore and solid phases were segmented using Otsu thresholding. Subsequently, image analysis was used to extract quantitative parameters, such as porosity, surface-to-volume ratio (S/V), and tortuosity. To estimate the surface area of pore spaces, the *skimage.measure* module from the scikit-image package in Python was used. First, the marching cubes algorithm (Lewiner et al., 2003) was applied to extract the triangulated iso-surface from the 3D volumetric data. Then, the function *mesh_surface_area* (van der Walt et al., 2014) of the same module was used to compute the total surface area of the resulting mesh. To estimate the tortuosity, the *TauFactor* (Kench et al., 2023) module in Python was used.

2.6. Data Integration

To ensure consistent spatial comparison across imaging modalities, the MRI and XRCT data were first co-registered based on two reference features. First, the three reference tubes embedded in the sample holder (Section 2.1) provided fixed markers for lateral and rotational alignment. Second, the top and bottom edges of the sand pack were used for axial alignment. The axial origin was defined as the position immediately downstream of the inlet tissue. To reconcile the substantial difference in native voxel resolution between XRCT (8 μm) and MRI (0.14 mm in-plane, 0.5 mm slice thickness), both data sets were resampled to the scale of a representative elementary volume (REV). This REV scale was determined from XRCT data by evaluating how the key structural descriptors (porosity, tortuosity, and mean pore diameter) stabilized with increasing sample volume. For this analysis, cubic sub-volumes with side lengths between 0.9 and 1.5 mm were extracted from the clean (untreated) sand column. Porosity was computed directly from the binary segmentation and the mean pore diameter was estimated using the SNOW (Sub-Network of Watersheds) partitioning algorithm implemented in the *PoreSpy* library (Gostick, 2017). Across all three structural descriptors, values fluctuated at small cube sizes but stabilized once the cube side exceeded approximately 1.3–1.4 mm (Figure S2 in Supporting Information S1). Beyond this threshold, changes in porosity, tortuosity, and mean pore diameter were <2%, indicating that structural properties had reached scale-independent behavior. Based on this convergence, a cube size of 1.38 mm was selected as the REV size. This REV size provides statistically stable structural properties while preserving sufficient spatial resolution to resolve axial heterogeneity in precipitation.

MRI-derived T_1 and T_2 relaxation times profiles were averaged over five vertical slices per segment, while volumetric water content was averaged over 27 vertical slices to ensure full cross-sectional coverage. We first averaged parameters over vertical slices to ensure full coverage, and then calculate averages for 14 axial segments based on the XRCT-derived REV scale. XRCT-derived porosity, surface-to-volume ratio (S/V), and tortuosity were calculated for the same 14 axial segments.

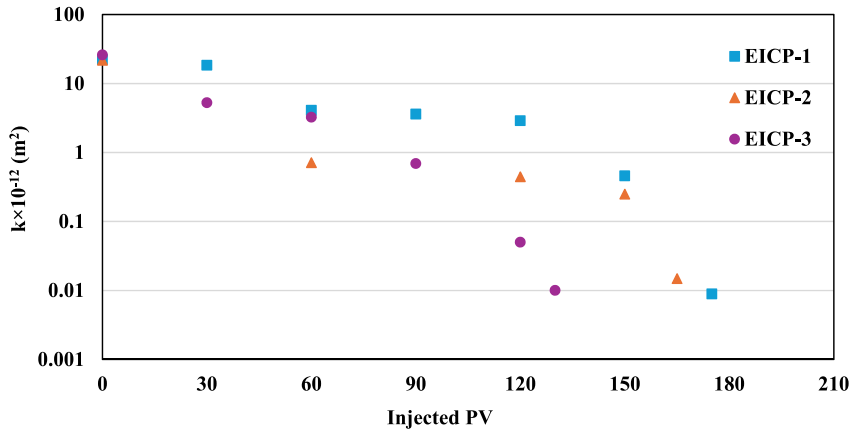


Figure 3. Development of the intrinsic permeability (m^2) as a function of injected pore volumes (PV) for the three replicate experiments.

3. Results and Discussion

3.1. Permeability Measurements

The initial intrinsic permeability of the three replicate samples (EICP-1, EICP-2, EICP-3) ranged between 22.1×10^{-12} and 25.9×10^{-12} m^2. Bulk porosity ϕ ranged from 0.37 to 0.38 cm^3 cm^{-3} based on the mass balance and known dimensions of the samples. This value is consistent with values typically reported for uniformly graded quartz sands of similar grain size, confirming the reliability of the packing procedure (Bear, 2013). Because this baseline was acquired after the initial permeability characterization (Section 2.1), it reflects the packed structure following initial exposure to flow, allowing subsequent structural changes to be attributed to EICP treatment rather than flow-induced rearrangement. The remaining differences reflect slight variations in packing density and pore geometry. Such variability is inherent to granular systems and underscores the need for replication.

During the course of EICP treatment, all samples exhibited a strong and progressive decline in permeability (Figure 3). For EICP-1, permeability decreased from 22.1×10^{-12} m^2 to 0.0089×10^{-12} m^2 after injection of 175 PV. For EICP-2, the permeability was reduced to 0.0148×10^{-12} m^2 after 165 PV, and for EICP-3 the permeability decreased from 25.9×10^{-12} m^2 to 0.010×10^{-12} m^2 after 130 PV. Despite the slightly different initial conditions, all replicates showed a similar order-of-magnitude decrease. Detailed information on the temporal development of the permeability for all three replicates is provided in Table S1 of Supporting Information S1.

The pressure evolution during injection mirrored this permeability loss for EICP-1, with increasing injection pressures observed in successive cycles (Figure 4). Notably, the pressure at the start of each injection cycle was typically lower than that at the end of the previous cycle, indicating partial relaxation of hydraulic resistance after flow cessation during the periods for MRI and XRCT measurements (see timeline in Figure 2). This relaxation likely reflects the transformation of amorphous calcium carbonate (ACC) into crystalline polymorphs such as vaterite and calcite, which is accompanied by water release, structural consolidation, and a reduction in the volume of precipitates (Zhang et al., 2021). To exclude the possibility that this relaxation was due to extensive sample handling and flow variation during permeability determination, a separate control experiment using the same column and packing procedure was conducted without sample handling between injection periods and permeability testing. The results for this control experiment also showed pressure relaxation in no-flow periods, indicating that this behavior cannot be attributed to particle mobilization from sample handling or flow-rate variations during permeability determination. The injection timelines for the two replicates are presented in Figures S3 and S4 of Supporting Information S1 and also confirm this general behavior. We therefore conclude that the transient pressure dynamics are related to the interplay between pore-scale precipitation, ACC transformation, and resulting flow resistance.

19447973, 2026, 11, Downloaded from https://agupubs.onlinelibrary.wiley.com/doi/10.1029/2026WR044004 by Sander Huisman - Forschungszentrum Juelich Gmbh , Wiley Online Library on [01/11/2026]. See the Terms and Conditions (https://onlinelibrary.wiley.com/terms-and-conditions) on Wiley Online Library for rules of use; OA articles are governed by the applicable Creative Commons License

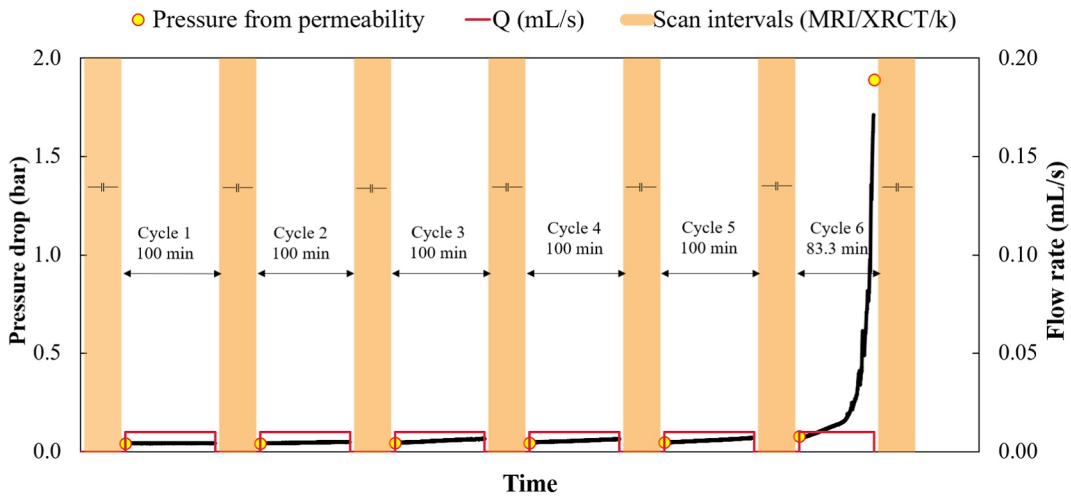


Figure 4. Injection timeline for EICP-1 showing pressure development (left axis) during injection with a constant flow rate (right axis), and intervals of MRI, XRCT, and permeability measurements (shaded). The yellow dots indicate the estimated ΔP at $Q = 0.01$ mL s^{-1} based on an extrapolation of the pressure measurements acquired for the permeability determination after each injection cycle.

3.2. MRI Results

MRI provided information on water distribution and relaxation dynamics during EICP treatment. Figure 5 shows processed images of the central slice after successive injection cycles for EICP-1. The corresponding results for

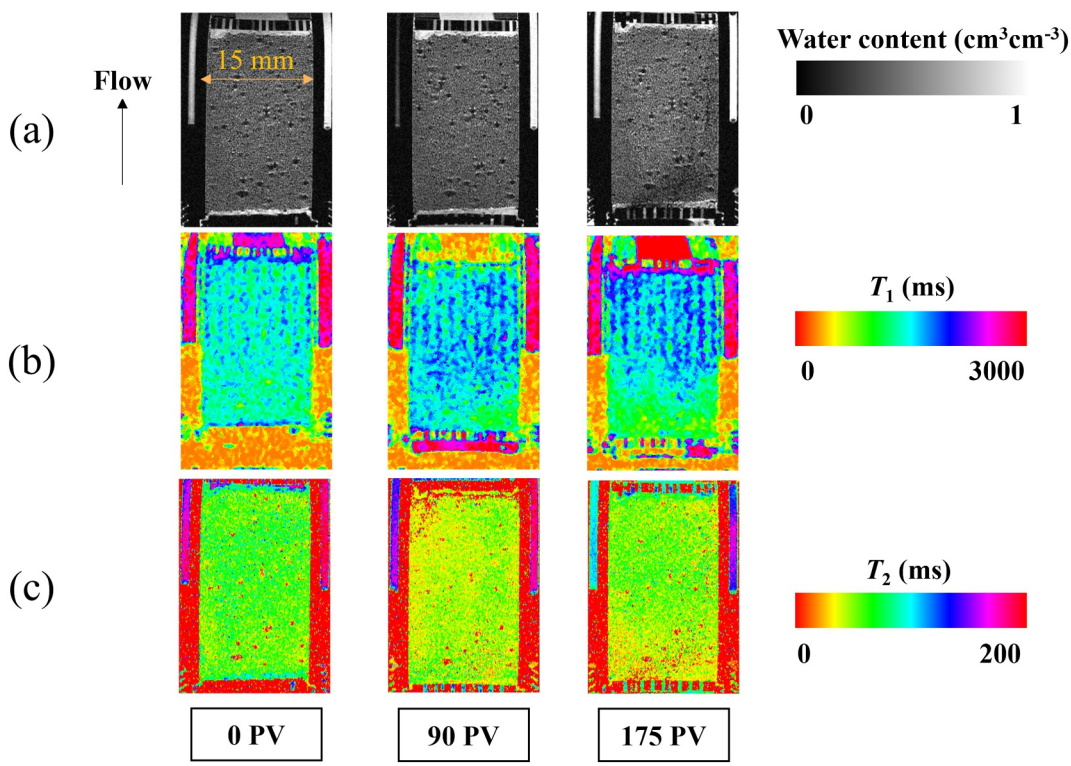


Figure 5. Results of the MRI monitoring of EICP during constant flow injection for a vertical slice of 0.5 mm thickness through the center of the EICP-1 sample. The FOV is 20 × 36 mm^2 and the resolution is 0.14 mm^2. The bright strips on the left and right are the reference tubes filled with water and cementing solution, respectively. The bright region at the top is the outflow compartment and the comb-like structures at the ends represent the perforated plates. (a) Water content maps normalized to the reference tube with known water content. (b) T_1 relaxation maps, and (c) T_2 relaxation maps.

19447973, 2026, 11, Downloaded from https://agupubs.onlinelibrary.wiley.com/doi/10.1029/2026WR044004 by Sander Huisman - Forschungszentrum Juelich Gmbh , Wiley Online Library on [01/11/2026]. See the Terms and Conditions (https://onlinelibrary.wiley.com/terms-and-conditions) on Wiley Online Library for rules of use; OA articles are governed by the applicable Creative Commons License

19447973, 2026, 11, Downloaded from https://agupubs.onlinelibrary.wiley.com/doi/10.1029/2026WR044004 by Sander Huisman - Forschungszentrum Juelich Gmbh , Wiley Online Library on [01/11/2026]. See the Terms and Conditions (https://onlinelibrary.wiley.com/terms-and-conditions) on Wiley Online Library for rules of use; OA articles are governed by the applicable Creative Commons License

EICP-2 and EICP-3 are provided in Figures S5 and S6 of Supporting Information S1. Across all three replicates, the water content maps (Figure 5a; Figures S5a and S6a in Supporting Information S1) show the same qualitative progression: the column remains initially homogeneous, followed by the emergence of a low water content zone near the inlet that intensifies with injected pore volume. In EICP-1, progressive darkening near the inlet became evident after ~90 PV, consistent with localized loss of water-filled pore space due to $CaCO_3$ precipitation. While the spatial extent and contrast of this inlet-localized signal vary between replicates, reflecting stochastic precipitation and small packing differences, the direction of change is consistent and aligns with the permeability reductions measured after each injection cycle.

The T_1 relaxation maps (Figure 5b) showed localized decreases in the same region. Because T_1 is primarily governed by interactions between hydrogen nuclei of pore water with the pore walls as indicated by the surface relaxation term in Equation 2, shorter T_1 times reflect increased surface-to-volume ratios caused by pore narrowing due to new mineral–water interfaces. This is confirmed by the simultaneous reduction of T_1 and volumetric water content. The progressive reduction in T_1 values near the inlet therefore indicates shrinkage of larger pores. Similar inlet localized changes in T_1 were observed in EICP-2 and EICP-3 (Figures S5 and S6 in Supporting Information S1), although the onset cycle and magnitude varied between replicates.

The T_2 relaxation maps (Figure 5c) exhibited more spatially uniform changes, with an overall trend toward shorter values across the column. Unlike T_1, the T_2 relaxation time is influenced by both surface relaxation and diffusion of water molecules in internal magnetic field gradients that arise from magnetic susceptibility contrasts between the solid grains and the pore fluid. The magnitude of these effects depends on pore size and geometry, the roughness and chemistry of the pore walls, and the mobility of water within the pore network (Arns et al., 2011; Hussain et al., 2014). In systems undergoing precipitation, these factors change simultaneously, which makes quantitative interpretation of T_2 challenging. Nevertheless, the overall uniform decline in T_2 suggests that precipitation was not only restricted to regions near the inlet, but also introduced distributed microstructural changes throughout the sample. Together, the MRI-derived parameters indicate that $CaCO_3$ precipitation initiated local, progressively narrowing pores (shorter T_1), and altered relaxation dynamics across the column (shorter T_2), confirming pore-scale restructuring during EICP. Across replicates, T_2 showed the same overall trend toward shorter values.

3.3. XRCT Results

XRCT imaging provides quantitative information on the evolution of pore structure during EICP treatment. Segmentation of the reconstructed volumes showed that pore-space reduction became discernible after approximately 90 PV of injection and intensified with continued treatment for all three samples. The segmented images for EICP-1 (Figure 6a) illustrate the progressive transition from an initially homogeneous pore structure toward a more heterogeneous distribution of solid and void phases, with increasing solid fraction near the injection inlet. The magnified pore-scale views (Figure 6b) highlight changes at the grain scale. While the pore network at 0 PV appears well connected with open intergranular voids, the close-up after 90 PV indicates partial narrowing of pore constrictions. After 175 PV, a substantial fraction of the pore space is occupied by precipitated solids. At the column scale, minor densification is visible in the lower region after 90 PV for EICP-1, whereas the solid phase becomes markedly more continuous near the inlet after 175 PV, indicating substantial pore filling (Figure 6a). To quantify these changes, the porosity loss was evaluated in $1.38 \times 1.38 \times 1.38$ mm^3 REVs (Figure 6c). The results show a heterogeneous pattern of porosity reduction, with the largest local decreases occurring near the inlet (i.e., from 0.37 to 0.24 cm^3 cm^{-3}) and smaller reductions further upstream. Overall, the XRCT analysis confirms a spatially non-uniform precipitation process that preferentially reduced pore volume near the inlet.

3.4. Joint Interpretation of MRI and XRCT

To quantify variations in porosity and to achieve a joint interpretation, we analyzed vertical profiles derived from XRCT and MRI (Figures 7a and 7b). The XRCT-based porosity profiles (Figure 7a) confirmed a strong reduction near the injection inlet, where porosity decreased by up to 0.10 cm^3 cm^{-3}, while the upper part of the column remained nearly unchanged. The average porosity of the entire sample declined from 0.35 to 0.28 cm^3 cm^{-3}. Independent material balance calculations yielded an initial porosity of 0.38 cm^3 cm^{-3}, which is in good agreement with the XRCT-derived value (error <0.03 cm^3 cm^{-3}). MRI-derived water-content profiles (Figure 7b) showed the same overall trend, with reduced water content near the inlet but smoother spatial variation. The

10.1029/2026WR044004

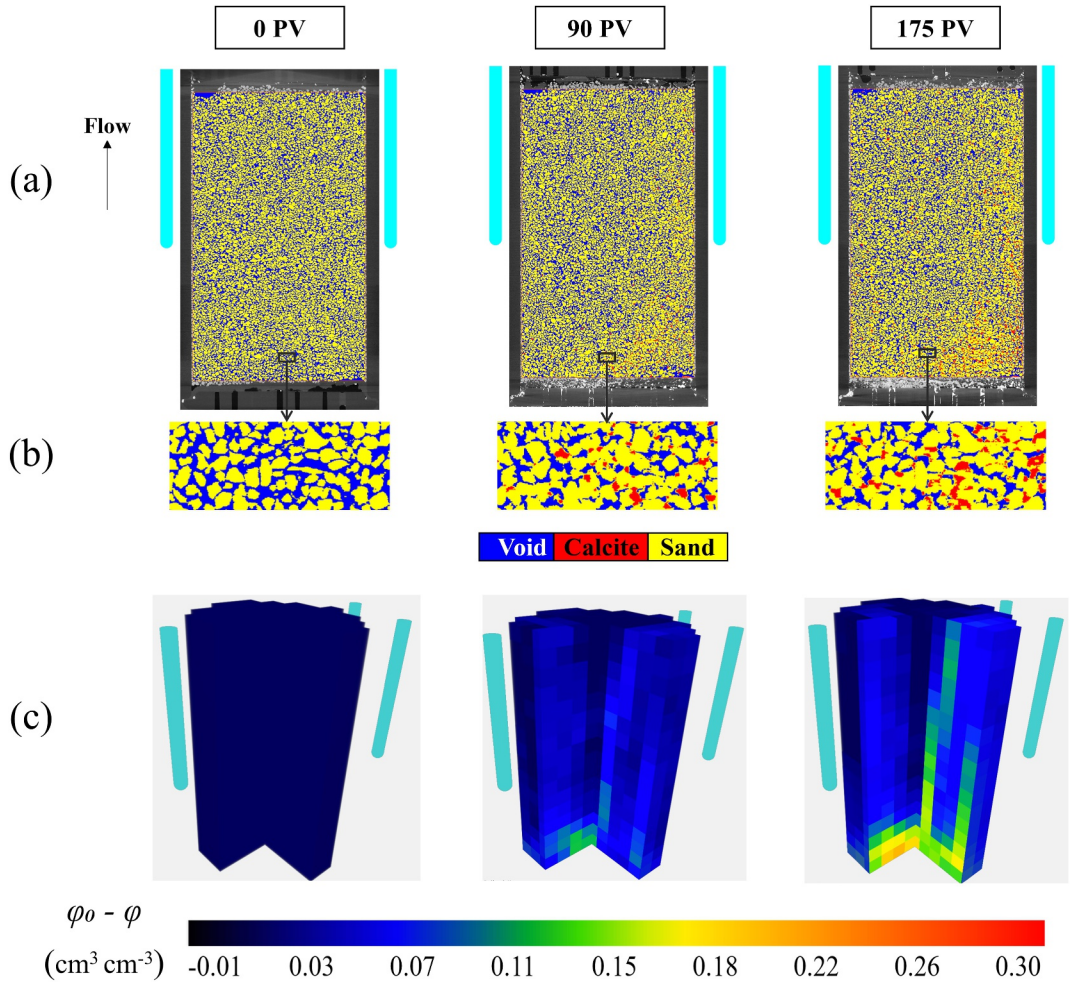


Figure 6. (a) XRCT segmentation results showing pore-structure evolution during EICP-1. A central slice through the sample shows the sand, calcite and void phase before injection (0 PV) and after 90 and 175 PV. (b) Enlarged view of a representative segmented region. (c) Absolute reduction in porosity (φ_0–φ, $cm^3\ cm^{-3}$) computed from 1.38 mm^3 representative elementary volumes (REVs), showing spatial distribution of porosity reduction. Please note that the color scale in Figure 6c is fixed from −0.01 to 0.30 $cm^3 cm^{-3}$ across panels for visual comparability. It does not represent the maximum observed change in porosity.

average water content decreased from 0.36 to 0.30 $cm^3\ cm^{-3}$ over the course of the experiment. The close agreement between MRI and XRCT validates both imaging methods and shows that precipitation predominantly initiated at the inlet and propagated in axial direction. The mean residence time across the column (~140–162 s; Table S2 in Supporting Information S1) is short relative to timescales over which substantial ureolysis-driven reactant consumption has been reported in similar systems. Using the first-order ureolysis rate coefficient reported for the same jack bean meal concentration (2.5 g L^{-1}; Feder et al., 2021; Hommel et al., 2020; von Wolff et al., 2021), the effective first-order rate constant is $k_{eff} \approx 6.5 \times 10^{-4}\ s^{-1}$. For the estimated residence time, this means that only ~9%-10% of urea and Ca^{+2} are expected to be consumed per single pass through the column, indicating that reactants remained available along the full column length on any given pass. Based on substrate availability alone, this would suggest a more spatially homogeneous precipitation pattern than observed. The pronounced inlet-localization seen here is therefore better explained by progressive retention of urease and amorphous calcium carbonate (ACC) at pore throats near the inlet over successive injection cycles, which locally enhances reaction and precipitation rates there, rather than by depletion of reactants along the column length.

Across the three replicate experiments, the axial shape of the porosity and water-content profiles was highly consistent (Figures S7 and S8 in Supporting Information S1), with all samples exhibiting inlet-localized porosity reduction and limited changes in the upper column. The reductions in average column porosity were 0.07, 0.18

19447973, 2026, 11, Downloaded from https://agupubs.onlinelibrary.wiley.com/doi/10.1029/2026WR044004 by Sander Huisman - Forschungszentrum Juelich Gmbh , Wiley Online Library on [01/11/2026]. See the Terms and Conditions (https://onlinelibrary.wiley.com/terms-and-conditions) on Wiley Online Library for rules of use; OA articles are governed by the applicable Creative Commons License

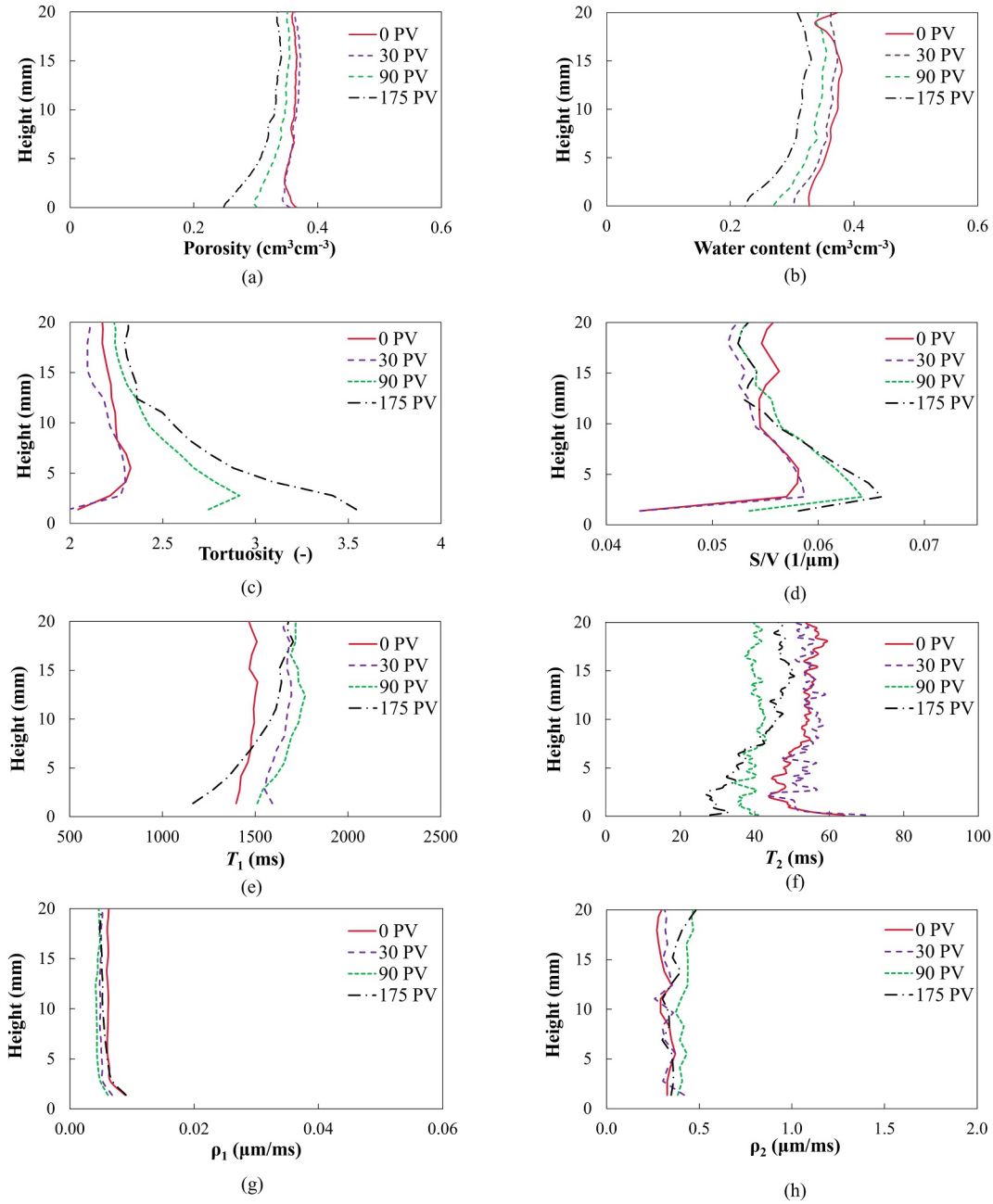


Figure 7. Vertical profiles obtained from non-invasive imaging of EICP-1 for selected injection cycles. All profiles show values averaged over the vertical REV (1.38 mm) height. (a) XRCT-derived porosity profiles, (b) MRI-derived water content profiles, (c) XRCT-derived tortuosity profiles, (d) XRCT-derived surface-to-volume ratio (S/V) profiles, (e) MRI-derived T_1 relaxation profiles, (f) MRI-derived T_2 relaxation profiles, (g, h) surface relaxivities for T_1 and T_2 processes, respectively.

and 0.10 $cm^3\ cm^{-3}$ for EICP-1, EICP-2, and EICP-3, respectively. These differences likely arise from a combination of factors intrinsic to EICP systems. Small variations in initial packing density and local pore connectivity can alter flow redistribution during early injection cycles, amplifying spatial heterogeneity in precipitation. In addition, EICP is known to be sensitive to enzyme activity, local substrate availability, and transient formation of amorphous calcium carbonate (ACC), which introduces stochasticity in nucleation and growth processes. Similar levels of replicate-to-replicate variability under otherwise identical conditions have been reported in previous EICP studies (Weinhardt et al., 2022), reflecting the inherently heterogeneous and kinetically controlled nature of biomineralization in porous media. Despite this variability, the reproducible axial pattern observed here

19447973, 2026, 11, Downloaded from https://agupubs.onlinelibrary.wiley.com/doi/10.1029/2026WR044004 by Sander Huisman - Forschungszentrum Juelich Gmbh , Wiley Online Library on [01/11/2026]. See the Terms and Conditions (https://onlinelibrary.wiley.com/terms-and-conditions) on Wiley Online Library for rules of use; OA articles are governed by the applicable Creative Commons License

19447973, 2026, 11, Downloaded from https://agupubs.onlinelibrary.wiley.com/doi/10.1029/2026WR044004 by Sander Huisman - Forschungszentrum Juelich Gmbh , Wiley Online Library on [01/11/2026]. See the Terms and Conditions (https://onlinelibrary.wiley.com/terms-and-conditions) on Wiley Online Library for rules of use; OA articles are governed by the applicable Creative Commons License

demonstrates that the dominant spatial evolution of precipitation is robust under constant flow injection. The remaining apparent differences between MRI and XRCT measurements on the same sample reflect both methodological and physical factors. XRCT resolves pore-space geometry at micrometer resolution (~8 μm), while MRI integrates over larger voxel volumes and is influenced by relaxation effects. As a result, XRCT captures sharp porosity gradients, whereas MRI provides spatially averaged information on the water-filled pore space. The general agreement between XRCT-based porosity and MRI-based water content also implies that microporosity plays no role, since this would be manifested in higher water contents in MRI because MRI also detects water in small pores that are not resolved in XRCT.

The combined analysis of MRI relaxation data (T_1, T_2) and XRCT-derived microstructural parameters (tortuosity and S/V) is used to obtain a coherent picture of how precipitation in the pore space evolved during the EICP experiments. The XRCT-derived S/V increased slightly from ~0.058 μm^{-1} to ~0.063 μm^{-1} near the inlet, while remaining nearly unchanged downstream (Figure 7e). This corresponds to a decrease in the average pore-body radius ($r_{av} = 2\ V/S$) from ~34 to ~32 μm. These XRCT-derived S/V closely matched independent measurements obtained by NMR diffusometry for F32 sand (0.057 μm^{-1}; Duschl et al., 2015), supporting the reliability of our XRCT segmentation. Tortuosity showed a more pronounced response than S/V during the early injection cycles (0–90 PV). In the lower 5 mm of the column, tortuosity increased from ~2.2 to ~2.7, while remaining nearly constant in the upper regions. This response indicates that early precipitation primarily affected pore connectivity rather than uniformly modifying pore-wall surface area. At the same time, only a modest local porosity reduction (~0.023 $cm^3\ cm^{-3}$) was observed near the inlet after 90 PV, while the column-averaged porosity decreased by only ~4%. The limited reduction in porosity and the substantial increase in tortuosity suggest that early permeability loss is governed by connectivity reduction rather than bulk pore filling.

Pore throats represent geometrical constrictions that control hydraulic connectivity and can dominate permeability in granular porous media (Bear, 2013). Even limited mineral deposition at these locations can strongly increase flow-path length and redirection, leading to a disproportionate rise in tortuosity while bulk porosity remains largely unchanged (Hommel et al., 2018). A possible explanation for preferential precipitation in pore throats during EICP is the formation of amorphous calcium carbonate (ACC), which may be transported as a suspended phase and preferentially retained at these constrictions through mechanical trapping/straining, analogous to deep-bed filtration of particle-laden flows in porous media.

MRI relaxation data further support the notion of an early decrease in connectivity. T_2 values decreased uniformly by a small amount during the early injection cycles, reflecting the strong influence of internal magnetic field gradients arising from susceptibility differences between quartz grains and pore water. Because paramagnetic impurities in F32 sand reside mostly inside the sand grains (Weinhardt et al., 2022), the effective T_2 is controlled chiefly by diffusion in these internal gradients rather than by direct interaction of water molecules with the surface. Thus, early precipitation only weakly affects T_2. In contrast, T_1 showed a distinct and spatially localized increase during the first injection cycles (0–90 PV). The surface relaxivity ρ_1, which was calculated from the T_1 and XRCT-derived S/V profiles by appropriate reformulation of Equation 3, remained nearly constant (Figure 7g). This is explained as follows. Generally, surface relaxivity of T_1 is controlled by the molecular reorientation in combination with adsorption/desorption processes at the surface (Mitchell et al., 2010). Thus, T_1 is relatively long since pores are large and surface relaxivity is low. There is rapid diffusional exchange possible between narrow pores or throats, where local relaxation is faster according to Equation 2. The diffusional length during T_1 (~130 μm) is sufficient to probe the full pore body. Thus, rapid exchange between throats and bulk pores leads to averaging, explaining the observed monomodal relaxation. We assume now that initial precipitation proceeded mainly in the throats so that relaxation there ceased and only slower bulk relaxation persisted. This explains the slight increase in T_1 relaxation time until 90 PVs, and further supports an early loss of connectivity at the pore-throat scale.

After ~90 PV, XRCT showed that structural changes intensified and expanded beyond the inlet region. Both tortuosity and S/V increased more sharply, particularly within the bottom 5–7 mm of the column. Tortuosity exceeded 3.0 in this region by the final cycle, indicating that flow paths became substantially longer and more tortuous. In parallel, S/V increased from 0.058 to ~0.065 μm^{-1}, consistent with progressive coating, roughening, and partial infilling of pores as calcite crystals grow. This is consistent with the MRI results, where T_1 began to decrease after ~90 PV after an initial increase. This shift reflects the growing influence of surface relaxation as pore bodies contract and the effective S/V increases. The invariance of ρ_1 confirms that this decrease in T_1 is

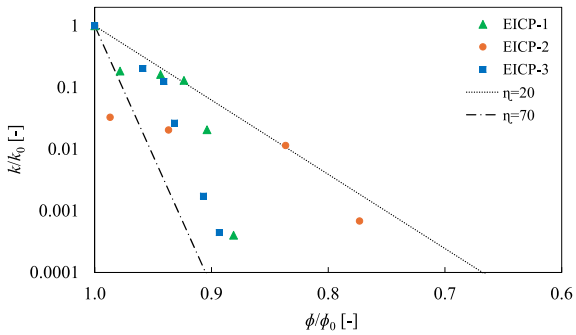


Figure 8. Relationship between normalized permeability (k/k_0) and normalized porosity (φ/φ_0) during constant flow rate injection for three replicate experiments (EICP-1, EICP-2, EICP-3) and the envelope of possible power-law relationships describing the data with an η range from 20 to 70 at the sample scale.

caused by geometric changes rather than changes in surface chemistry. T_2 also decreases further throughout the column, with increased spatial variability, reflecting stronger confinement and enhanced internal gradient effects as precipitation thickens. Overall, MRI and XRCT jointly indicate that the system evolves from localized pore-throat clogging (connectivity loss) to distributed pore-body constriction (increased S/V and reduced pore volume) as injection proceeds. As a summary of the experimental results, the initial and final structural properties (e.g., S/V, tortuosity) of all replicates are presented in Table S2 of Supporting Information S1 together with a summary of other key experimental parameters.

3.5. Porosity-Permeability Relationships

In a final step, the relationship between normalized permeability (k/k_0) and normalized mean porosity (ϕ/ϕ_0) is interpreted in the context of the precipitation development derived from the joint interpretation of MRI and XRCT (Figure 8). Across all three replicates, permeability decreased by more than three orders of magnitude while the column-averaged porosity was reduced by less than 40%, demonstrating a strongly nonlinear sensitivity of flow capacity to precipitation. It is important to emphasize that the presented k/k_0–ϕ/ϕ_0 trends at the sample scale are governed by both microstructural changes (e.g., pore-throat narrowing, increased tortuosity, and changes in surface geometry) and the macroscopic distribution of precipitation along the column (i.e., inlet-localized vs. more distributed precipitation), since a localized low-porosity zone can dominate the hydraulic response even when the bulk porosity remains relatively high. In addition, the use of a constant flow rate for injection can result in lateral variability in calcite precipitation because preferential flow paths may remain open, as previously reported for microfluidic experiments with EICP (Weinhardt et al., 2022).

All three experiments showed a pronounced permeability decrease already at the early stages of treatment, when the bulk porosity remained high $\phi/\phi_0 > 0.9$. This behavior is consistent with the joint interpretation of the MRI and XRCT results, which suggested that the early permeability loss is driven primarily by loss of hydraulic connectivity (throat impairment and path elongation) rather than by uniform filling of pore bodies across the sample. With further precipitation ($\phi/\phi_0 < 0.8$), permeability approached values close to the detection limit (i.e., $k/k_0 \approx 10^{-3}$) consistent with the development of strongly impaired flow zones in the lower part of the column, as resolved by both MRI and XRCT.

Although the three replicates used identical injection protocols, their porosity-permeability trajectories differ quantitatively, reflecting sensitivity of EICP to local precipitation patterns and pore-network connectivity. A widely used power-law relationship to describe experimental data is given by:

$$\frac{k}{k_0} = (\varnothing/\varnothing_0)^{\eta}, \tag{5}$$

where η is a fitting parameter (Hommel et al., 2018). To summarize the variability in the porosity-permeability relationships, Figure 8 shows the envelope of possible power-law relationships describing the data. The values for η range from 20 to 70 at the sample scale. These values fall at the extreme end of those summarized by Bernabé et al. (2003), matching only their highest-reported category (dissolution in sedimentary rocks, $\eta > 20$) and the disconnection-related behavior they note for plastic compaction and sintering at low porosity, rather than the more moderate exponents ($\eta \approx 2$–20) typical of most processes in their compilation. We attribute this to a difference in mechanism: most processes summarized by Bernabé et al. (2003) involve relatively distributed pore-space modification, whereas the present system undergoes a connectivity-collapse process in which a small number of pore throats disproportionately control sample-scale flow behavior consistent with approaching a local percolation threshold, and qualitatively similar to the disconnection effects noted for plastic compaction and sintering in their compilation. Specifically, flow becomes controlled by localized low-porosity zones near the inlet in the later stages of the experiments, such that the bulk permeability responds primarily to the minimum effective porosity along the flow path rather than to the column-averaged porosity. This is reflected in the lower magnitude and reduced range of values for η (10–45) when the porosity of the lower 5 mm of the sample is considered instead of the mean porosity of the entire sample. The reduced sample length used here, relative to the

19447973, 2026, 11, Downloaded from https://agupubs.onlinelibrary.wiley.com/doi/10.1029/2026WR044004 by Sander Huisman - Forschungszentrum Juelich GmbH , Wiley Online Library on [01/11/2026]. See the Terms and Conditions (https://onlinelibrary.wiley.com/terms-and-conditions) on Wiley Online Library for rules of use; OA articles are governed by the applicable Creative Commons License

19447973, 2026, 11, Downloaded from https://agupubs.onlinelibrary.wiley.com/doi/10.1029/2026WR044004 by Sander Huisman - Forschungszentrum Juelich Gmbh , Wiley Online Library on [01/11/2026]. See the Terms and Conditions (https://onlinelibrary.wiley.com/terms-and-conditions) on Wiley Online Library for rules of use; OA articles are governed by the applicable Creative Commons License

larger rock-core samples typically underlying such compilations, further limits flow-path redundancy and amplifies the sensitivity of bulk permeability to localized clogging, compounding the connectivity-collapse effect described above. Together, these factors illustrate the impact of the scale mismatch between porosity and bulk permeability reduction that is common to many studies dealing with porosity-permeability relationships for reactive transport problems.

The non-invasive imaging data suggest that the observed spread in the porosity-permeability data is not purely stochastic. Already after 90 PV, structural changes within the bottom 5 mm near the inlet differed substantially between replicates. For example, porosity decreased from 0.38 to 0.35 in EICP-1, from 0.35 to 0.28 in EICP-2, and from 0.40 to 0.34 in EICP-3. Over the same region, XRCT-derived tortuosity increased from 2.00 to 2.19 for EICP-1, from 2.22 to 2.77 for EICP-2, and from 2.13 to 2.37 for EICP-3. While these local differences in porosity reduction and connectivity loss are consistent with the observed spread in k/k_0–φ/φ_0 behavior, it remains challenging to uniquely relate porosity and permeability across replicates. For example, the early drop in EICP-2 is likely associated with a strong initial decrease in permeability associated with increased tortuosity. The subsequent moderate decrease in permeability is associated with a more homogeneous evolution of the precipitation distribution between 90 and 120 PV. Overall, the results indicate that permeability evolution during EICP is controlled by a combination of factors, including the spatial extent, connectivity, and continuity of clogging zones, rather than by any single geometric descriptor alone. Taken together, these results demonstrate that bulk, column-averaged porosity is a poor predictor of permeability evolution whenever precipitation is spatially heterogeneous, a condition common to EICP and MICP systems generally, and one that limits the practical value of a single sample-scale power-law exponent for this class of problem. Critically, however, this limitation is not irreducible: when the porosity metric is chosen to reflect the local, flow-limiting zone rather than the bulk average, the predictive relationship tightens substantially (η: 10–45 vs. 20–70). This indicates that the apparent breakdown of porosity-permeability relationships at the sample scale is not evidence that porosity and permeability are decoupled, but rather that meaningful prediction requires spatially-resolved structural information, connectivity, local minimum porosity, and precipitation distribution, rather than bulk averages alone. This is precisely the gap that combined MRI–XRCT characterization, as demonstrated in this study, is positioned to fill, and points toward incorporating spatially-resolved or connectivity-based descriptors into porosity-permeability models for reactive transport applications, rather than relying on bulk power-law fits calibrated to column-averaged porosity (Wang et al., 2024).

4. Conclusions

This study demonstrates the potential of coupling magnetic resonance imaging (MRI) and X-ray computed tomography (XRCT) to resolve structure-transport relationships during enzyme-induced calcite precipitation (EICP) at the representative elementary volume (REV) scale. Constant flow rate injection produced more than three orders of magnitude reduction of permeability, with precipitation initiating near the inlet and progressing axially through the column. MRI provided dynamic information on water content and relaxation times (T_1, T_2), revealing localized pore constriction and progressive reduction of mobile water. XRCT complemented these observations by quantifying porosity, tortuosity, and surface-to-volume ratio, thereby linking pore-scale structural changes to macroscopic transport properties. Together, the dual imaging approach showed that permeability loss was not simply proportional to porosity reduction. Progressive narrowing and, in places, closure of pore throats reduced the number of available flow pathways, the primary driver of permeability loss, which was reflected structurally in increased tortuosity (path elongation) and increased surface-to-volume ratio, consistent with progressive modification of pore surfaces by precipitate coating.

By integrating complementary imaging modalities with hydraulic measurements, this work provides a robust framework for characterizing the spatiotemporal dynamics of EICP at the representative elementary volume (REV) scale. In particular, the identification of pore-throat connectivity loss as the dominant early control on permeability, distinct from bulk porosity reduction, provides mechanistic detail directly relevant to pore-network and Darcy-scale reactive transport models that explicitly represent throat clogging (e.g., Schollenberger et al., 2024). In particular, the presented results can inform the choice of structural descriptors used to parameterize permeability evolution in such models. More broadly, our results highlight the value of multi-modal non-invasive imaging for resolving coupled structural and hydraulic evolution in porous media undergoing reactive transport.

Conflict of Interest

The authors declare no conflicts of interest relevant to this study.

Availability Statement

All data sets generated and analyzed in this study, including processed XRCT segmentation results, MRI relaxation maps (T_1, T_2), water-content distributions, porosity, tortuosity and *S/V* profiles, and permeability measurements, are publicly available through the DaRUS research data repository of the University of Stuttgart (Emadi et al., 2026; https://doi.org/10.18419/DARUS-5650). Due to the large size of raw XRCT data sets, these files are archived locally. The raw data or intermediate processing files are available from the corresponding author upon reasonable request.

Acknowledgments
This study was financially supported by the Deutsche Forschungsgemeinschaft (DFG, German Research Foundation)—Project Number 327154368—SFB 1313. The authors gratefully acknowledge Jörg Stellbrink for his assistance with the viscosity measurements. They also wish to thank Matthias Ruf, Felix Weinhardt, Kerem Bozkurt, Johannes Hommel, Holger Class, Robin Gerlach, and Holger Steeb for valuable discussions, technical support, and insightful advice throughout this work. Open Access funding enabled and organized by Projekt DEAL.

References

Ahenkorah, I., Rahman, M. M., Karim, M. R., & Teasdale, P. R. (2020). A comparison of mechanical responses for microbial- and enzyme-induced cemented sand. *Géotechnique Letters*, *10*(4), 559–567. https://doi.org/10.1680/jgele.20.00061

Almajed, A., Khodadadi Tirkolaei, H., & Kavazanjian, E., Jr. (2018). Baseline investigation on enzyme-induced calcium carbonate precipitation. *Journal of Geotechnical and Geoenvironmental Engineering*, *144*(11), 04018081. https://doi.org/10.1061/(asce)gt.1943-5606.0001973

Arab, M. G., Alsodi, R., Almajed, A., Yasuhara, H., Zeiada, W., & Shahin, M. A. (2021). State-of-the-art review of enzyme-induced calcite precipitation (EICP) for ground improvement: Applications and prospects. *Geosciences*, *11*(12), 492. https://doi.org/10.3390/geosciences11120492

Arns, C. H., AlGhamdi, T., & Arns, J. Y. (2011). Numerical analysis of nuclear magnetic resonance relaxation-diffusion responses of sedimentary rock. *New Journal of Physics*, *13*(1), 015004. https://doi.org/10.1088/1367-2630/13/1/015004

Bear, J. (2013). *Dynamics of fluids in porous media, courier Corporation*. North Chelmsford.

Bernabé, Y., Mok, U., & Evans, B. (2003). Permeability-porosity relationships in rocks subjected to various evolution processes. *Pure and Applied Geophysics*, *160*(5–6), 937–960. https://doi.org/10.1007/pl00012574

Bray, J. M., Lauchnor, E. G., Redden, G. D., Gerlach, R., Fujita, Y., Codd, S. L., & Seymour, J. D. (2017). Impact of mineral precipitation on flow and mixing in porous media determined by micro-computed tomography and MRI. *Environmental Science & Technology*, *51*(3), 1562–1569. https://doi.org/10.1021/acs.est.6b02999

Brownstein, K. R., & Tarr, C. E. (1979). Importance of classical diffusion in NMR studies of water in biological cells. *Physical Review A*, *19*(6), 2446–2453. https://doi.org/10.1103/physreva.19.2446

Cheng, L., & Cord-Ruwisch, R. (2014). Upscaling effects of soil improvement by microbially induced calcite precipitation by surface percolation. *Geomicrobiology Journal*, *31*(5), 396–406. https://doi.org/10.1080/01490451.2013.836579

Cheng, L., Shahin, M. A., & Mujah, D. (2017). Influence of key environmental conditions on microbially induced cementation for soil stabilization. *Journal of Geotechnical and Geoenvironmental Engineering*, *143*(1), 04016083. https://doi.org/10.1061/(asce)gt.1943-5606.0001586

Cnudde, V., & Boone, M. N. (2013). High-resolution X-ray computed tomography in geosciences: A review of the current technology and applications. *Earth-Science Reviews*, *123*, 1–17. https://doi.org/10.1016/j.earscirev.2013.04.003

Cuthbert, M. O., McMillan, L. A., Handley-Sidhu, S., Riley, M. S., Tobler, D. J., & Phoenix, V. R. (2013). A field and modeling study of fractured rock permeability reduction using microbially induced calcite precipitation. *Environmental Science & Technology*, *47*(23), 13637–13643. https://doi.org/10.1021/es402601g

DeJong, J. T., Mortensen, B. M., Martinez, B. C., & Nelson, D. C. (2010). Bio-mediated soil improvement. *Ecological Engineering*, *36*(2), 197–210. https://doi.org/10.1016/j.ecoleng.2008.12.029

DeJong, J. T., Soga, K., Kavazanjian, E., Burns, S., van Paassen, L. A., Al Qabany, A., et al. (2014). Biogeochemical processes and geotechnical applications: Progress, opportunities and challenges. In *Bio- and chemo-mechanical processes in geotechnical engineering: Géotechnique symposium in print 2013* (pp. 143–157). ICE Publishing.

Duschl, M., Galvosas, P., Brox, T. I., Pohlmeier, A., & Vereecken, H. (2015). In situ determination of surface relaxivities for unconsolidated sediments. *Water Resources Research*, *51*(8), 6549–6563. https://doi.org/10.1002/2014wr016574

Edzes, H. T., Van Dusschoten, D., & Van As, H. (1998). Quantitative T2 imaging of plant tissues by means of multi-echo MRI microscopy. *Magnetic Resonance Imaging*, *16*(2), 185–196.

Emadi, S., Bakhshi, P., Pohlmeier, A., & Huisman, J. A. (2026). Coupling MRI and XRCT to resolve structure-transport evolution during enzyme-induced calcite precipitation at the REV scale [Dataset]. *DaRUS*. https://doi.org/10.18419/DARUS-5650

Feder, M. J., Akyel, A., Morasko, V. J., Gerlach, R., & Phillips, A. J. (2021). Temperature-dependent inactivation and catalysis rates of plant-based ureases for engineered biomineralization. *Engineering Reports*, *3*(2), e12299. https://doi.org/10.1002/eng2.12299

Fridjonsson, E. O., Seymour, J. D., Schultz, L. N., Gerlach, R., Cunningham, A. B., & Codd, S. L. (2011). NMR measurement of hydrodynamic dispersion in porous media subject to biofilm mediated precipitation reactions. *Journal of Contaminant Hydrology*, *120*, 79–88. https://doi.org/10.1016/j.jconhyd.2010.07.009

Gostick, J. T. (2017). Versatile and efficient pore network extraction method using marker-based watershed segmentation [software]. *Physical Review E*, *96*(2), 023307. https://doi.org/10.1103/physreve.96.023307

Guan, K. M., Nazarova, M., Guo, B., Tchelepi, H., Kovscek, A. R., & Creux, P. (2019). Effects of image resolution on sandstone porosity and permeability as obtained from X-ray microscopy. *Transport in Porous Media*, *127*(1), 233–245. https://doi.org/10.1007/s11242-018-1189-9

Haber-Pohlmeier, S., Caterina, D., Blümich, B., & Pohlmeier, A. (2021). Magnetic resonance imaging of water content and flow processes in natural soils by pulse sequences with ultrashort detection. *Molecules*, *26*(17), 5130. https://doi.org/10.3390/molecules26175130

Handley-Sidhu, S., Sham, E., Cuthbert, M. O., Nougarol, S., Mantle, M., Johns, M. L., et al. (2013). Kinetics of urease mediated calcite precipitation and permeability reduction of porous media evidenced by magnetic resonance imaging. *International Journal of Environmental Science and Technology*, *10*(5), 881–890. https://doi.org/10.1007/s13762-013-0241-0

Hommel, J., Akyel, A., Frieling, Z., Phillips, A. J., Gerlach, R., Cunningham, A. B., & Class, H. (2020). A numerical model for enzymatically induced calcium carbonate precipitation. *Applied Sciences*, *10*(13), 4538. https://doi.org/10.3390/app10134538

19447973, 2026, 11, Downloaded from https://agupubs.onlinelibrary.wiley.com/doi/10.1029/2026WR044004 by Sander Huisman - Forschungszentrum Juelich Gmbh , Wiley Online Library on [01/11/2026]. See the Terms and Conditions (https://onlinelibrary.wiley.com/terms-and-conditions) on Wiley Online Library for rules of use; OA articles are governed by the applicable Creative Commons License

Hommel, J., Coltman, E., & Class, H. (2018). Porosity-permeability relations for evolving pore space: A review with a focus on (bio-) geochemically altered porous media. *Transport in Porous Media*, *124*(2), 589–629. https://doi.org/10.1007/s11242-018-1086-2

Hommel, J., Gehring, L., Weinhardt, F., Ruf, M., & Steeb, H. (2022). Effects of enzymatically induced carbonate precipitation on capillary pressure-saturation relations. *Minerals*, *12*(10), 1186. https://doi.org/10.3390/min12101186

Hu, W., Cheng, W.-C., Wen, S., & Yuan, K. (2021). Revealing the enhancement and degradation mechanisms affecting the performance of carbonate precipitation in EICP process. *Frontiers in Bioengineering and Biotechnology*, *9*, 750258. https://doi.org/10.3389/fbioe.2021.750258

Hussain, F., Pinczewski, W. V., Cinar, Y., Arns, J.-Y., Arns, C. H., & Turner, M. L. (2014). Computation of relative permeability from imaged fluid distributions at the pore scale. *Transport in Porous Media*, *104*(1), 91–107. https://doi.org/10.1007/s11242-014-0322-7

Kakelar, M. M., Ebrahimi, S., & Hosseini, M. (2016). Improvement in soil grouting by biocementation through injection method. *Asia-Pacific Journal of Chemical Engineering*, *11*(6), 930–938. https://doi.org/10.1002/apj.2027

Kavazanjian, E., & Hamdan, N. (2015). Enzyme induced carbonate precipitation (EICP) columns for ground improvement. In *Ifcee 2015* (pp. 2252–2261).

Kench, S., Squires, I., & Cooper, S. (2023). TauFactor 2: A GPU accelerated python tool for microstructural analysis [Software]. *Journal of Open Source Software*, *8*(88), 5358. https://doi.org/10.21105/joss.05358

Kirkland, C. M., Norton, D., Firth, O., Eldring, J., Cunningham, A. B., Gerlach, R., & Phillips, A. J. (2019). Visualizing MICP with X-ray μ-CT to enhance cement defect sealing. *International Journal of Greenhouse Gas Control*, *86*, 93–100. https://doi.org/10.1016/j.ijggc.2019.04.019

Kirkland, C. M., Zanetti, S., Grunewald, E., Walsh, D. O., Codd, S. L., & Phillips, A. J. (2017). Detecting microbially induced calcite precipitation in a model well-bore using downhole low-field NMR. *Environmental Science & Technology*, *51*(3), 1537–1543. https://doi.org/10.1021/acs.est.6b04833

Krajewska, B. (2018). Urease-aided calcium carbonate mineralization for engineering applications: A review. *Journal of Advanced Research*, *13*, 59–67. https://doi.org/10.1016/j.jare.2017.10.009

Kwon, T. H., Ham, S. M., Baek, S. H., Han, G., Martinez, A., & DeJong, J. (2024). Pore-scale precipitation pattern and grain-scale cementation strength by microbially induced calcium carbonate precipitation (MICP). In *E3S Web of Conferences* (Vol. 544, p. 01013). EDP Sciences. https://doi.org/10.1051/e3sconf/202454401013

Lewiner, T., Lopes, H., Vieira, A. W., & Tavares, G. (2003). Efficient implementation of marching cubes' cases with topological guarantees. *The Journal of Graphics Tools*, *8*(2), 1–15. https://doi.org/10.1080/10867651.2003.10487582

Mitchell, J., Chandrasekera, T. C., & Gladden, L. F. (2010). Obtaining true transverse relaxation time distributions in high-field NMR measurements of saturated porous media: Removing the influence of internal gradients. *The Journal of Chemical Physics*, *132*(24), 244705. https://doi.org/10.1063/1.3446805

Nemati, M., & Voordouw, G. (2003). Modification of porous media permeability using calcium carbonate produced enzymatically in situ. *Enzyme and Microbial Technology*, *33*(5), 635–642. https://doi.org/10.1016/s0141-0229(03)00191-1

Nitz, W. (1999). Principles of magnetic resonance imaging and magnetic resonance angiography. In *Clinical MR imaging: A practical approach* (pp. 1–35). Springer Berlin Heidelberg.

Salek, M. F., & Beckingham, L. E. (2023). Effect of X-ray computed tomography imaging parameters on quantification of petrophysical properties. *Earth and Space Science*, *10*(10), e2023EA003095. https://doi.org/10.1029/2023ea003095

Saxena, N., Hows, A., Hofmann, R., Alpak, F. O., Freeman, J., Hunter, S., & Appel, M. (2018). Imaging and computational considerations for image computed permeability: Operating envelope of digital rock physics. *Advances in Water Resources*, *116*, 127–144. https://doi.org/10.1016/j.advwatres.2018.04.001

Schindelin, J., Arganda-Carreras, I., Frise, E., Kaynig, V., Longair, M., Pietzsch, T., et al. (2012). Fiji: An open-source platform for biological-image analysis [Software]. *Nature Methods*, *9*(7), 676–682. https://doi.org/10.1038/nmeth.2019

Schollenberger, T., von Wolff, L., Bringedal, C., Pop, I. S., Rohde, C., & Helmig, R. (2024). Investigation of different throat concepts for precipitation processes in saturated pore-network models. *Transport in Porous Media*, *151*(14), 2647–2692. https://doi.org/10.1007/s11242-024-02125-5

Sham, E., Mantle, M. D., Mitchell, J., Tobler, D. J., Phoenix, V. R., & Johns, M. L. (2013). Monitoring bacterially induced calcite precipitation in porous media using magnetic resonance imaging and flow measurements. *Journal of Contaminant Hydrology*, *152*, 35–43. https://doi.org/10.1016/j.jconhyd.2013.06.003

Thrane, L. W., Daily, R. L., Thane, A., Kirkland, C. M., McCarney, E. R., Dykstra, R., et al. (2020). Detecting microbially induced calcium carbonate precipitation in porous systems using low-field nuclear magnetic resonance relaxometry. *Journal of Geotechnical and Geoenvironmental Engineering*, *146*(4), 04020012. https://doi.org/10.1061/(asce)gt.1943-5606.0002226

van der Walt, S., Schönberger, J. L., Nunez-Iglesias, J., Boulogne, F., Warner, J. D., Yager, N., et al. (2014). Scikit-image: Image processing in python [Software]. *PeerJ*, *2*, e453. and the scikit-image contributors. https://doi.org/10.7717/peerj.453

von Wolff, L., Weinhardt, F., Class, H., Hommel, J., & Rohde, C. (2021). Investigation of crystal growth in enzymatically induced calcite precipitation by micro-fluidic experimental methods and comparison with mathematical modeling. *Transport in Porous Media*, *137*(2), 327–343. https://doi.org/10.1007/s11242-021-01560-y

Wang, Z., Hu, M., & Steefel, C. (2024). Pore-scale modeling of reactive transport with coupled mineral dissolution and precipitation. *Water Resources Research*, *60*(6), e2023WR036122. https://doi.org/10.1029/2023wr036122

Weinhardt, F., Deng, J., Hommel, J., Dastjerdi, S. V., Gerlach, R., Steeb, H., & Class, H. (2022). Spatiotemporal distribution of precipitates and mineral phase transition during biomineralization affect porosity-permeability relationships: Microfluidic investigations. *Transport in Porous Media*, *143*(2), 527–549. https://doi.org/10.1007/s11242-022-01782-8

Wildenschild, D., & Sheppard, A. P. (2013). X-ray imaging and analysis techniques for quantifying pore-scale structure and processes in subsurface porous medium systems. *Advances in Water Resources*, *51*, 217–246. https://doi.org/10.1016/j.advwatres.2012.07.018

Willett, M. R., Bedey, K., Crandall, D., Seymour, J. D., Rutqvist, J., Cunningham, A. B., et al. (2024). Beyond the surface: Non-invasive low-field NMR analysis of microbially induced calcium carbonate precipitation in shale fractures. *Rock Mechanics and Rock Engineering*, *59*(5), 1–20. https://doi.org/10.1007/s00603-024-04052-9

Yang, E., Baek, S., Kwon, T. H., & Yun, T. S. (2024). X-ray CT-based interpretation of microbial-induced carbonate precipitation and local hydraulic behaviors. *Engineering Geology*, *330*, 107426. https://doi.org/10.1016/j.enggeo.2024.107426

Yasuhara, H., Neupane, D., Hayashi, K., & Okamura, M. (2012). Experiments and predictions of physical properties of sand cemented by enzymatically induced carbonate precipitation. *Soils and Foundations*, *52*(3), 539–549. https://doi.org/10.1016/j.sandf.2012.05.011

Zhang, G., Du, P., Zhong, J., Bao, Y., Xu, Z., Lu, J., & Li, Y. Y. (2021). Supervariate ceramics: Biomineralization mechanism. *Materials Today Advances*, *10*, 100144. https://doi.org/10.1016/j.mtadv.2021.100144

Zhang, Q., Ye, W., Liu, Z., Wang, Q., & Chen, Y. (2023). Influence of injection methods on calcareous sand cementation by EICP technique. *Construction and Building Materials*, *363*, 129724. https://doi.org/10.1016/j.conbuildmat.2022.129724

19447973, 2026, 11, Downloaded from https://agupubs.onlinelibrary.wiley.com/doi/10.1029/2026WR044004 by Sander Huisman - Forschungszentrum Juelich Gmbh , Wiley Online Library on [01/11/2026]. See the Terms and Conditions (https://onlinelibrary.wiley.com/terms-and-conditions) on Wiley Online Library for rules of use; OA articles are governed by the applicable Creative Commons License